water

MDPI

Article

Flood Risk Prediction Framework Considering Combined Effects of Rainfall, Tide and Land Surface Changes Under a Non-Stationary Environment in a Coastal City

Hongshi Xu, Jiahao Zhang, Huiliang Wang *, Yongle Guan, Yuhe Deng and Yongjie Zhou

School of Water Conservancy and Transportation, Zhengzhou University, Zhengzhou 450001, China
* Correspondence: wanghuiliang@zzu.edu.cn

Abstract

Coastal cities are prone to flooding due to extreme rainfall, rising sea levels, and urbanization. This study develops a non-stationary flood risk prediction framework for a coastal city to assess the combined effects of rainfall, tide, and land surface change on future flood inundation and socioeconomic risk. Future rainfall was predicted by integrating the time-varying parameter distribution (TVPD) model with CMIP6 data through a genetic algorithm; future tides were estimated using the TVPD model; and land use in 2035 was simulated using the Markov–PLUS model. Flood inundation and the associated socioeconomic risks were then evaluated. The results showed that the integrated rainfall prediction approach reduced RMSE by 13.4% compared with the individual models. The land use simulation also showed acceptable performance, with a Kappa coefficient of 0.79 and an FOM value of 0.15. Under the combined effects of rainfall, tide, and land use change, the future peak inundation volume increased by 19.97% on average relative to the baseline period, while the affected population and economic losses increased by 72,603 people and US$12.61 billion, respectively. These results indicate that flood risk in coastal cities may be substantially exacerbated under a non-stationary environment, and the proposed framework can provide support for future flood risk assessment and adaptation planning.

Keywords: flood risk; climate change; land use change; hydrological–hydrodynamic model

1. Introduction

Floods are among the most frequent natural disasters worldwide, causing devastating loss to life and property. Currently, one-quarter of the global population is exposed to 100-year flood risk, with 70% concentrated in East and South Asia [1]. Coastal cities are prone to flooding due to extreme rainfall, rising sea levels, and urbanization [2]. Under climate change, coastal cities are experiencing increasing trends in rainfall and tides [3]. For instance, the global mean relative sea level has risen at a rate of 2.6 mm/year over the past two decades [4]. Moreover, as hubs of economic activity and dense populations due to urbanization, coastal cities face severe losses when subjected to flooding [5].

Future flood risk is usually predicted by integrating hydrological–hydrodynamic models with future rainfall, tide, and land surface conditions in coastal cities [6]. And copula-based methods have been widely used to characterize the joint dependence among multiple flood drivers, such as extreme precipitation, storm surge, tide, and river discharge, providing improved estimates of joint exceedance probabilities and enabling assessment of compound flood hazards in coastal cities [7,8]. Machine learning and deep learning

Check for updates

Academic Editor: Gwo-Fong Lin

Received: 15 April 2026
Revised: 15 May 2026
Accepted: 16 May 2026
Published: 20 May 2026

Copyright: © 2026 by the authors. Licensee MDPI, Basel, Switzerland. This article is an open access article distributed under the terms and conditions of the Creative Commons Attribution (CC BY) license.

techniques, including LSTM, random forest, and hybrid models, have increasingly been applied for rapid flood prediction, urban inundation mapping, and compound flood forecasting, demonstrating strong predictive performance and computational efficiency in case studies such as coastal urban areas in China and Europe [9,10]. Previous studies have mainly focused on regional flooding caused by the interaction between heavy rainfall and tides or between heavy rainfall and river flooding [11] or urban waterlogging driven by the combined effects of heavy rainfall and land use changes [12]. However, studies that simultaneously consider future changes in rainfall, tides, and land use remain limited. Rainfall and tides are the primary hazard-driving factors for flooding in coastal cities, while land use directly affects urban runoff responses. Together, these three elements constitute the key factors influencing flood risk in coastal cities. Neglecting the evolution of any one of them may result in an incomplete identification of risk.

Consequently, predicting future changes in rainfall, tides, and land use is a critical prerequisite for reliable flood risk predictions. Global climate models (GCMs) and the time-varying parameter distribution (TVPD) model [13] are employed to predict rainfall and tides in previous studies. The TVPD model is based on historical datasets, with distribution parameters assumed to be time-varying, and historical data extensively exploited by the TVPD model. However, it does not sufficiently consider future social development scenarios. GCMs are scientific computational frameworks designed to predict global climate change trajectories. The GCMs are employed to simulate climate evolution under divergent societal development scenarios [14] by integrating shared socioeconomic pathways (SSPs) with representative concentration pathways (RCPs). The different societal development scenarios are incorporated by GCMs in future rainfall prediction [15], whereas consideration of regional-scale historical data remains absent [16]. To our knowledge, integration of complementary strengths between the TVPD model and GCMs for future rainfall prediction remains limited in the existing study.

In addition to global climate change, urban flooding processes are also affected by land surface change due to urbanization [17,18]. Common simulation methods for land use change include the Future Land Use Simulation (FLUS) model, Cellular Automata–Markov Chain (CA-Markov) model, and the Patch-Generating Land Use Simulation (PLUS) model [19]. The PLUS model incorporates a threshold-decreasing mechanism and diffusion coefficients to actively generate seed patches, forming spatial land use through competitive diffusion [19,20]. Random forest is adopted to quantify driving factors in the PLUS model, resolving the black-box limitations inherent in traditional artificial neural networks (ANNs) used by the FLUS model. Therefore, the PLUS model has been widely applied in land-use change simulation and has demonstrated high effectiveness [21,22].

Despite substantial progress in coastal flood research, several limitations remain. First, existing studies have primarily focused on rainfall–tide interactions or rainfall–land use interactions separately, while integrated assessments that simultaneously consider changes in rainfall, tide, and land surface conditions remain limited. Second, future rainfall and tide prediction are often based on either non-stationary statistical models or climate model outputs alone, and approaches that combine their complementary strengths are still scarce. Third, many flood studies emphasize inundation hazard, whereas the spatial redistribution of exposure to socioeconomic vulnerabilities under future compound flooding has received comparatively less attention. Therefore, this study develops a predictive framework that jointly accounts for future changes in rainfall, tide, and land use, and further integrates projected socioeconomic changes in coastal cities. In doing so, it addresses the limitations of existing future coastal urban flood risk assessment frameworks, particularly their incomplete consideration of hazard-driving factors and flood-conditioning environments, as well as their limited attention to the socioeconomic risk implications of future flooding.

In light of these limitations, this study develops an integrated flood risk prediction framework for coastal cities under a non-stationary environment. The novelty of this study does not lie in proposing a single new hydrological, hydrodynamic, or land use model, but in establishing a coordinated framework that links future rainfall prediction, tide estimation, land use simulation, flood inundation modeling, and socioeconomic exposure assessments. Unlike previous studies that mainly examined rainfall–tide interactions, rainfall–river flooding, or rainfall–land use changes separately, the proposed framework simultaneously incorporates future changes in rainfall, tide, and land surface conditions. The main contributions are summarized as follows: (a) A prediction model of future rainfall and tides is proposed by integrating a time-varying parameter distribution model and CMIP6 data through a genetic algorithm. (b) We established a flood risk prediction framework for the combined effects of rainfall, tide and land surface changes on flood inundation and socioeconomic risk under a non-stationary environment. The rest of this paper is structured as follows. Section 2 outlines the methodological framework adopted in this study. Section 3 introduces the study area and the datasets employed. Section 4 presents and discusses the key findings. Finally, Section 5 summarizes the major conclusions.

2. Methods

The research framework is presented in Figure 1. First, the different future rainfall and tide levels were predicted by the TVPD model and CMIP6 data, respectively. The weight of integration for the TVPD model and CMIP6 data was determined by genetic algorithms (GAs). Second, future land use was predicted by the Markov–PLUS model. Third, urban flood inundation was simulated based on a personal computer storm water management model (PCSWMM). Fourth, 72 future period (2035) scenarios and 36 base period (2023) scenarios were established for analyzing the impact of rainfall, tide and land surface changes on flood inundation based on predicted rainfall, tide, and land use. Finally, the socioeconomic risks under future compound floods were predicted based on projected population, gross domestic product (GDP) distributions and urban inundation.

2.1. Prediction Model of Rainfall and Tide

2.1.1. Time-Varying Parameter Distribution Model

In this study, the Generalized Extreme Value (GEV) function was chosen to fit the distribution of rainfall and tides. The homogeneity and stationarity of hydrological sequences have been increasingly disrupted due to climate change and intensive human activities. This method assumes that distribution parameters vary temporally, thereby highlighting the impacts of climate change and other driving factors on hydrological variables. For example, the time-varying GEV distribution can be defined as follows [23]:

$$F(x, \mu_t, \sigma_t, \delta_t) = \exp\left[-\left(1 + \delta_t \frac{x - \mu_t}{\sigma_t}\right)^{-\frac{1}{\delta_t}}\right] \quad (1)$$

where $\mu_t, \sigma_t, \delta_t$ represent the time-varying location, scale and shape parameters, respectively.

In this study, we found that when the shape parameter was negative and showed a decreasing trend over time, incorporating it as a time-varying parameter tended to produce lower estimates of extreme quantiles, which may lead to an underestimation of extreme values. Therefore, when such behavior occurred, the shape parameter was not included as a time-varying parameter in this study, in order to avoid potential underestimation of the designed rainfall or tide series.

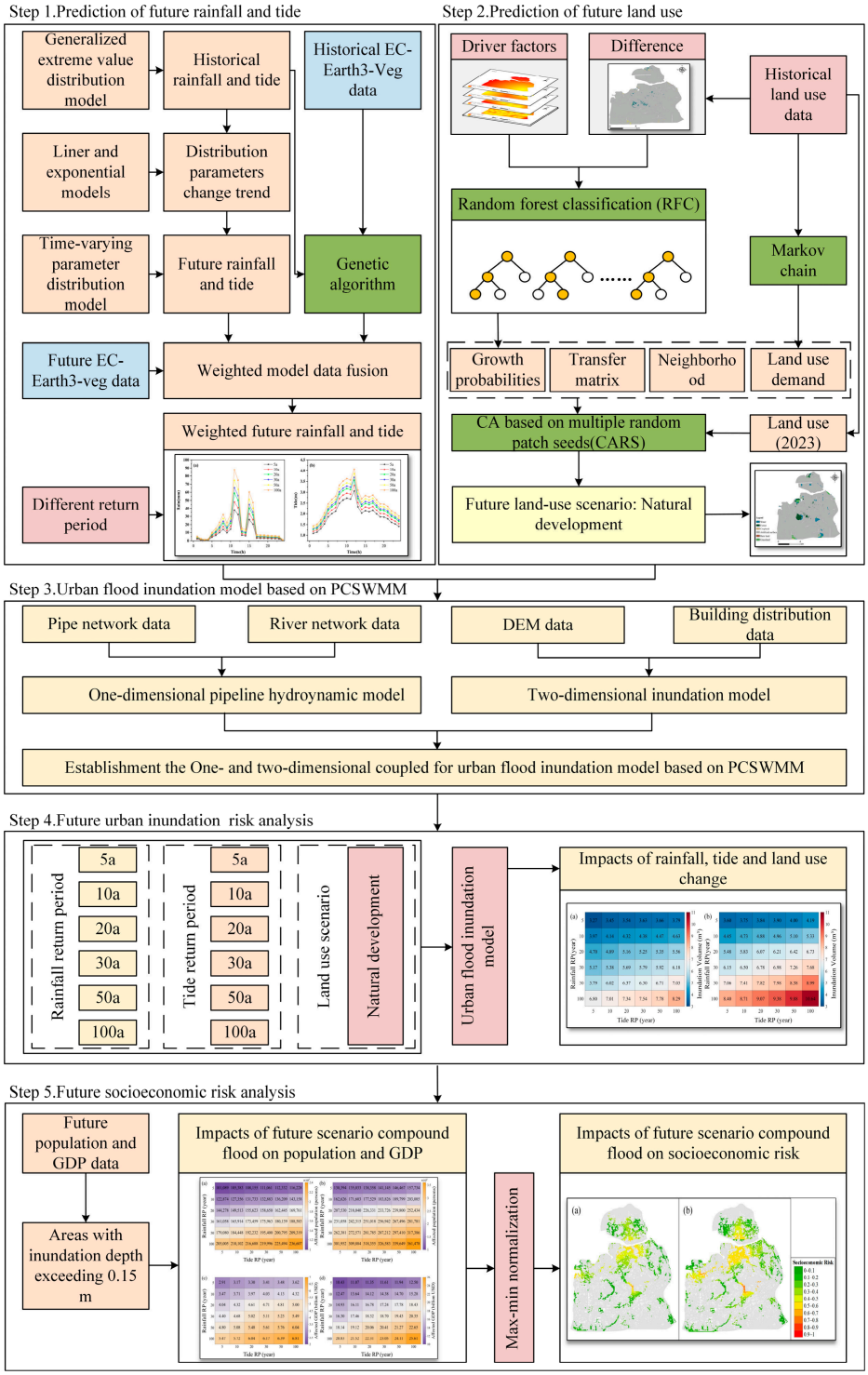

Figure 1. Flow chart used for flood risk prediction under a non-stationary environment.

It should also be noted that GEV-based prediction of rare extreme events is inherently uncertain, particularly for high-return-period rainfall and tide events. This uncertainty arises from limited sample sizes, parameter estimation errors, and extrapolation beyond the range of historical observations. Consequently, uncertainty in the estimated GEV parameters may propagate into the design rainfall and tide series, and further influence flood inundation simulation and socioeconomic risk assessment. In this study, the prediction intervals of the time-varying parameters were used to provide a preliminary representation of such uncertainty.

2.1.2. CMIP6 Data

In response to global climate change, the World Climate Research Program (WCRP) launched the Sixth International Coupled Model Intercomparison Program (CMIP6) to understand the mechanisms of climate change and project future trends by comparing simulation results from GCMs.

High-resolution CMIP6 downscaled daily Climate Projections over China (HiCPC), which is a novel dataset tailored to China's specific needs [15]. To address inherent biases in daily GCM simulations, this dataset used the China Meteorological Forcing Dataset (CMFD) as the reference, processed by an advanced bias correction and spatial disaggregation (BCSD) method.

The method is briefly outlined below: (1) Bias Correction: Observed rainfall data is remapped to align with the GCM grid. For each day of the year, values from both the GCMs and observed datasets are pooled within a ±15-day window to construct quantile mapping. Then, the GCM data points are transformed, correcting biases to match the distribution of the observed data. (2) Spatial Disaggregation: The coarse resolution GCM data is bilinearly interpolated to match the grid of the observation. The mean precipitation of each day of the year is calculated and employed as a scaling factor. These scaling factors are then applied to the prediction of daily interpolated GCMs by multiplication, resulting in downscaled GCM predictions.

2.1.3. Integration of the Time-Varying Parameter Distribution Model and CMIP6 Data

A genetic algorithm was employed to integrate the time-varying parameter distribution model with CMIP6 data in this study. First, cumulative probability distributions were derived from the rainfall series predicted by the time-varying parameter distribution model and the historical CMIP6 rainfall data, respectively. Then, the parameters of the GA were specified. The population size, maximum number of iterations, mutation rate, and crossover probability were set to 1000, 1000, 0.001, and 0.9, respectively. Subsequently, the GA was employed to assign weights to the two distributions. The root mean square error (RMSE) was employed as the fitness function to evaluate the performance of rainfall prediction after weight optimization in this study. A smaller RMSE indicated better agreement between the weighted prediction and the observed rainfall distribution. Through selection, crossover, and mutation operations, the GA iteratively searched for the near-optimal weight combination. Integration toward the optimal solution was achieved through progressive iteration increases, enabling a near-optimal weight for integrating the TVPD model and CMIP6 data. Finally, the near-optimal weight was assigned to the two model predictions to obtain the ultimate predicted rainfall. The weighting formula is as follows:

$$p = \sum_{i=1}^{n} w_i p_i \tag{2}$$

where p denotes the probability distribution after model weighting; p_i denotes the probability distribution of each model; and w_i denotes the corresponding weight of each model, with the sum of all weights equal to 1.

2.2. Prediction Model of Land Use

A recently developed model called PLUS was adopted to predict future land use in this study. The model was developed from the classical Cellular Automata (CA) model and is employed to predict the spatial and temporal evolution of complex systems. Depending on the realities of economic performance and planning scenarios, different scenarios can be designed to inform land use policy and land management decisions. Many studies have

shown that the PLUS model is very effective in predicting land use under the urbanization process. Thus, the established PLUS model was adopted to predict land use in the future.

As depicted in Figure 2, the PLUS model consists of two modules: the Land Expansion Analysis Strategy (LEAS) and the CA based on multiple types of random patch seeds (CARS). Growth probabilities are obtained from land expansion and driving factors using random forest classification in the LEAS module. Future land use is predicted by the CA model in the CARS module. And Kappa and FOM coefficients are assessed using the Kappa and FOM coefficients:

$$P_{ij} = \begin{bmatrix} P_{11} & \cdots & P_{1n} \\ \vdots & \ddots & \vdots \\ P_{n1} & \cdots & P_{nn} \end{bmatrix} \tag{3}$$

$$kappa = \frac{P_o - P_e}{1 - P_e} \tag{4}$$

where P_{ij} represents the land-use type before and after the transition, respectively. P_o is the ratio of the sum of the diagonal elements of the confusion matrix to the sum of all elements, and P_e is the sum of the products of the actual and predicted numbers for all classes divided by the square of the total number of samples.

$$FoM = \frac{B}{A + B + C + D} \tag{5}$$

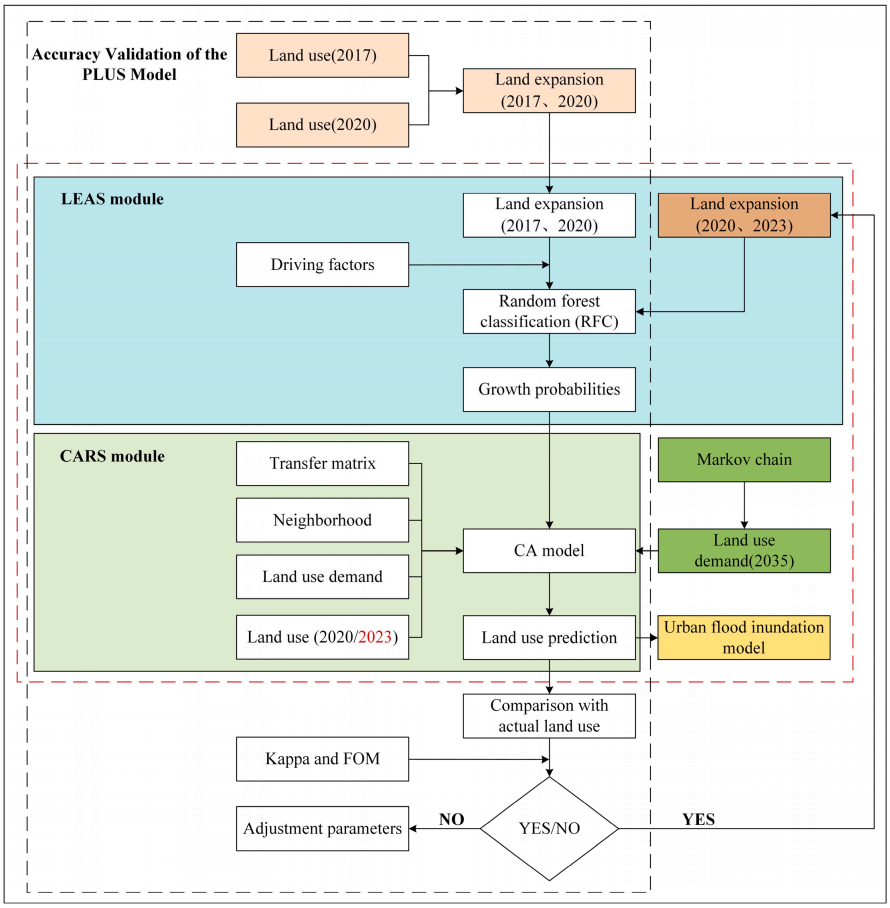

Figure 2. Flow chart used for land use prediction.

Here, A denotes the error area that actually changed but was predicted to be unchanged; B denotes the correctly predicted area that actually changed and was also predicted as changed; C denotes the error area where actual change and predicted change are inconsistent; and D denotes the error area that actually remained unchanged but was predicted to change.

2.3. Flood Risk Prediction Under a Non-Stationary Environment for a Coastal City

2.3.1. Designed Future Scenarios

In this study, the simulations of urban flood scenarios were divided into two periods: the base period (2023) and the future period (2035). The base period was determined based on available historical data. The future period was considered to be the period of future prediction of land use. The short-term (2035) was adopted for the predicted period of the framework due to increased uncertainty in land use driving factors under long-term prediction [24]. Urban inundation is predicted using designed land use scenarios and rainfall and tide levels for different return periods. The return periods of rainfall considered across 5–100 years are coupled with the tides of 5–100 years, with a 24 h duration. As shown in Table 1, 36 rainfall–tide combination scenarios were constructed for both base and future periods, respectively. Additionally, 36 scenarios were designed to simulate urban floods incorporating future land use changes.

Table 1. Design of future scenarios.

Scenario Type	Rainfall and Tide Scenario	Rainfall Return Period	Tide Return Period	Land Use Scenario
Base scenario	Current condition	5a, 10a, 20a, 30a, 50a, 100a	5a, 10a, 20a, 30a, 50a, 100a	Base period
Climate change scenario	Under future climate change	5a, 10a, 20a, 30a, 50a, 100a	5a, 10a, 20a, 30a 50a, 100a	Base period
Climate and land surface change scenario	Under future climate change	5a, 10a, 20a, 30a, 50a, 100a	5a, 10a, 20a, 30a, 50a, 100a	Future
Scenario type	Rainfall and tide scenario	Rainfall return period	Tide return period	Land use scenario

2.3.2. Flood Risk Prediction for Coastal Cities

(1) Urban flood inundation model

The urban flood inundation model includes a one-dimensional (1D) drainage model and a two-dimensional (2D) surface drainage model. The hydrodynamic calculation adopts the dynamic wave method, and the calculation formula is as follows:

$$\frac{\partial Q}{\partial x} + \frac{\partial A}{\partial t} = 0 \tag{6}$$

$$gA\frac{\partial H}{\partial x} + \frac{\partial}{\partial x}\left(\frac{Q^2}{A}\right) + \frac{\partial Q}{\partial t} + gAS_f = 0 \tag{7}$$

where A represents the cross-sectional area over water, m^2. H represents water depth, m. x represents distance along the conduit, m. Q represents the flow rate, m^3/s. t represents time, s. S_f represents the friction slope, and g represents gravity acceleration, m/s^2.

(2) Flood inundation and socioeconomic risk prediction

In this study, we examined the impact of rainfall, tide, and land changes on flooding inundation and socioeconomic risk. Flood inundation volume and extent were simulated by the urban flood inundation model. Then, we quantified the impacts of rainfall, tide, and land surface changes on future urban flood inundation by comparing the differences for 72 future scenarios and 36 base period scenarios.

Socioeconomic risk is one of the key dimensions for evaluating the impacts of flood disasters, mainly reflecting the direct threats and losses caused by flooding to population distribution and economic activities. In this study, the direct impacts of flooding on population and gross domestic product (GDP) were quantified using a spatial overlay analysis. Specifically, the simulated or observed flood inundation extent layers were overlaid with a high-resolution gridded population and GDP distribution data in ArcGIS10.8.1. Based on this overlay analysis, the population and GDP located within the inundated areas were extracted and calculated, and were used as estimates of the affected population and direct economic loss, respectively. As shown in Equation (8), the indices were obtained from population and GDP distributions based on the peak-minimum normalized technique:

$$N = \frac{X - X_{min}}{X_{max} - X_{min}} \tag{8}$$

where N denotes the normalized value; X denotes the grid value; and X_{max} and X_{min} are the peak and minimum values of the grid value, respectively.

Furthermore, to reflect the overall socioeconomic impact of flooding, the affected population index and affected GDP index were integrated to construct a socioeconomic risk index. The index was calculated as follows:

$$R_{se} = w_p I_p + w_g I_g \tag{9}$$

where R_{se} is the socioeconomic risk index; I_p is the affected population index; I_g is the affected GDP index; and w_p and w_g represent the weights of the affected population index and affected GDP index, respectively. The socioeconomic risk index can simultaneously reflect population exposure and economic vulnerability, thereby providing a more comprehensive description of regional socioeconomic risk under flood hazards.

3. Study Area and Data

3.1. Study Area

The proposed framework was applied in the main urban area of Haikou City, which is located in the north of Hainan Province, China (Figure 3). Haikou, the capital city of Hainan Province, is located at the northern edge of the low-latitude tropics and is bordered by the Qiongzhou Strait to the north, which is a typical tropical monsoon climate area. Bordering the South China Sea and the Pacific Ocean to the east, urban flooding in Haikou City has occurred frequently due to global warming and rising sea levels in recent years. For instance, Typhoon "Rammasun" made landfall in July 2014, causing rainfall of 505.5 mm and a high tide of 3.83 m [25]. This caused the deaths of eight people and losses that were worth nearly 1.43 billion dollars.

3.2. Data

The data utilized in this study are categorized into four components. The first part includes the data for rainfall and tides. The second part comprises data for urban land use simulations, such as historical land use and driving factor data. The third part involves foundational data, including DEM, drainage network data, and river channel data. The fourth part includes the prediction of population and GDP distributions. The sources and primary applications of the data are summarized in Table 2.

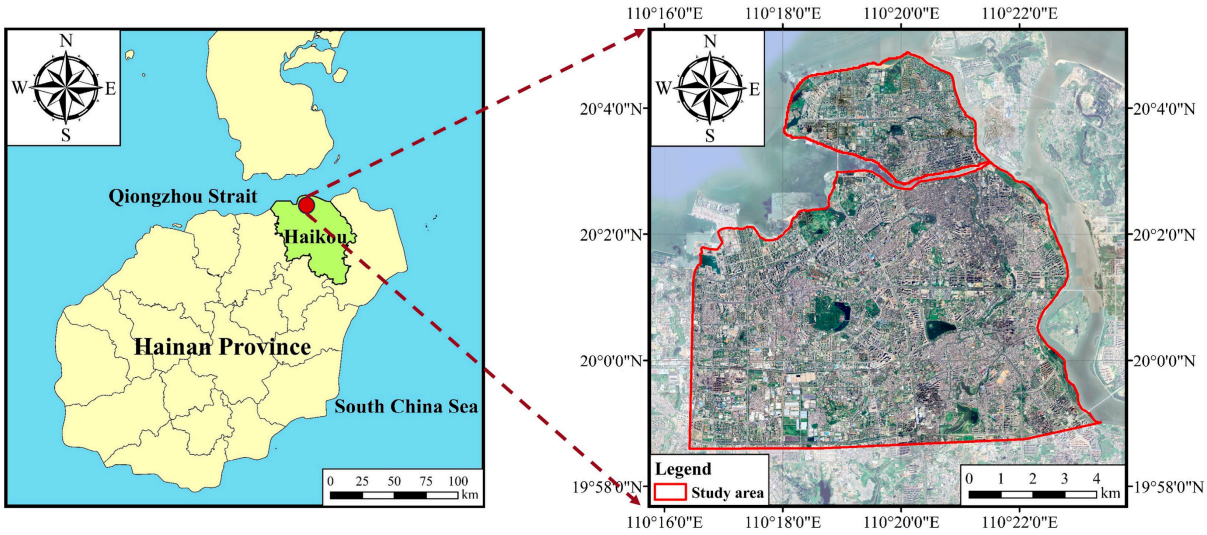

Figure 3. Location of the study area.

Table 2. Data sources and use.

No.	Data Type	Data Name	Data Use	Data Source
1	Rainfall and tides	Observed rainfall	Prediction of future rainfall and tide	Haikou Municipal Water Bureau
		Observed tide		
		Downscaled rainfall		https://doi.org/10.1038/s41597-024-03982-x [15], accessed on 13 January 2025.
2	Land use prediction	Observed land use	Land use expansion	European Space Agency (ESA) World Cover 10 m 2020 v100
		Natural Environment (DEM, Slope, and Aspect)	Land use driving factor	Resource and Environment Science and Data Center (https://www.resdc.cn/Default.aspx), accessed on 23 March 2025.
		Historical socioeconomic data		
		Roads		OSM Map Data
3	Urban flood inundation model	Pipe and river network data	Foundational data	Haikou Municipal Water Bureau
		Observed inundation	Calibration model parameters	
4	Socioeconomic data	Future socioeconomic data	Socioeconomic risk analysis	https://doi.org/10.6084/m9.figshare.19608594.v2 [26], accessed on 4 May 2025. and https://doi.org/10.5281/zenodo.5880037 [27], accessed on 12 May 2025.

4. Results and Discussion

4.1. Future Rainfall and Tide Prediction

4.1.1. Testing and Evaluation of Candidate Distribution Functions

To determine the optimal distribution for rainfall and tides, four candidate distributions, including the Generalized Extreme Value, lognormal, normal, and gamma distributions, were compared. The Kolmogorov–Smirnov (KS) test was applied to assess the goodness-of-fit, and additional evaluation metrics, including the Nash–Sutcliffe efficiency (NSE), relative error (RE), residual sum of squares (OLSs), and Akaike information criterion [7], were used for comprehensive comparison. With a significance level of $\alpha = 0.05$

and sample size of n = 39, the critical KS value was approximately 0.2178. As shown in Table 3, all candidate distributions passed the KS test. However, the GEV distribution demonstrated the best overall performance, yielding the highest NSE and the lowest RE, OLS, and AIC values.

Table 3. Testing of candidate distribution functions.

Type	Distribution	NSE	RE	OLS	AIC	KS
Rainfall	GEV	0.9897	0.0970	0.0304	−123.6377	0.0634
	Lognorm	0.9870	0.0985	0.0341	−116.5738	0.0717
	Norm	0.9355	0.2166	0.0761	−54.0011	0.1523
	Gamma	0.9764	0.1113	0.0460	−93.2096	0.0971
Tide	GEV	0.9794	0.1075	0.0414	−99.4787	0.1012
	Lognorm	0.9776	0.1089	0.0432	−98.1517	0.1148
	Norm	0.9620	0.1304	0.0563	−77.5475	0.1466
	Gamma	0.9748	0.1076	0.0458	−93.5668	0.1224

4.1.2. Model of Time-Varying Parameter Distribution for Rainfall and Tide

The GEV distribution was employed to fit historical rainfall and tide data from Haikou. In this study, the location and scale parameters are assumed to be a function of time under a non-stationary scenario, since long-term observations are lacking to determine the shape parameter [28]. As shown in Figure 4a,d, the trends of the shape parameter of rainfall and the scale parameter of tide are not significant, and the correlation coefficients, R^2, are lower than 0.4. For the other four distribution parameters, the correlation coefficients between fitted models all exceed 0.7, which indicates that the fitted models are reasonable. The linear and exponential fitted models are presented in Figure 4. Meanwhile, the prediction interval between 5% and 95% surrounds the time series of parameters, and reflects all possibilities of parameter changes, and thus can reasonably characterize the uncertainty of time-varying models. For rainfall, the location and scale parameters change with time, while the shape parameter remains unchanged. For tide, the location parameter changes with time, while the scale and shape parameters remain unchanged.

To evaluate the performance of the TVPD model, historical rainfall and tide data from 1974 to 2003 were used to develop non-stationary models, which were then employed to predict conditions in 2012. Figure 5 presents the predicted GEV distributions alongside the empirical distributions for both rainfall and tide. Overall, the non-stationary models show good agreement with the observed data, demonstrating the validity of the approach.

4.1.3. Integration of the TVPD Model with CMIP6 Data

The genetic algorithm was employed to integrate the TVPD model with CMIP6 data to enhance rainfall prediction accuracy under future scenarios. The genetic algorithm was configured with the following parameters: a population size of 1000, a maximum of 1000 iterations, a mutation rate of 0.001, and a crossover probability of 0.9. The EC-Earth3-Veg model under the SSP5-8.5 scenario was selected from the CMIP6 ensemble due to its superior capability in predicting rainfall over China [29]. Table 4 presents the weights assigned to the TVPD model and EC-Earth3-Veg model by the genetic algorithm, which are 0.839 and 0.161, respectively. Figure 6 shows the variation in the minimum RMSE during the model weighting process. Figure 7 shows the comparative performance between the weighted model and the individual models. In Figure 7a, the weighted model demonstrates enhanced alignment with the empirical distribution. Improved performance was observed across all metrics (as shown in Figure 7b), with the RMSE reduced by 13.4% from 11.73 mm to 10.16 mm. In this study, tide prediction was conducted with the TVPD model exclusively, due to the absence of a direct tide prediction in CMIP6. The 2014 Typhoon

Rammasun was widely referenced in the study area due to its destructive nature [30,31]. Consequently, the rainfall and tide processes during the 2014 Typhoon Rammasun were employed to inform the design of future rainfall and tides for different return periods in the future (as detailed in Figure 8).

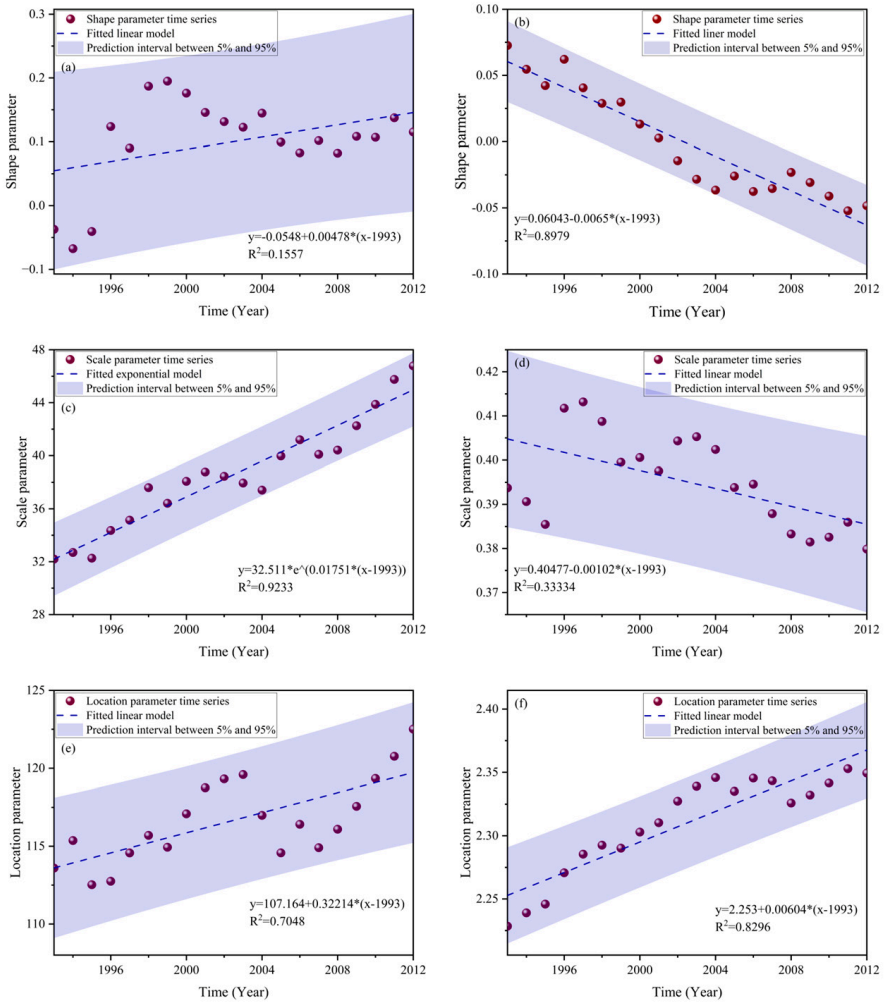

Figure 4. Variation trend of distribution parameters. (**a**) Shape parameter of rainfall. (**b**) Shape parameter of tide. (**c**) Scale parameter of rainfall. (**d**) Scale parameter of tide. (**e**) Location parameter of rainfall. (**f**) Location parameter of tide.

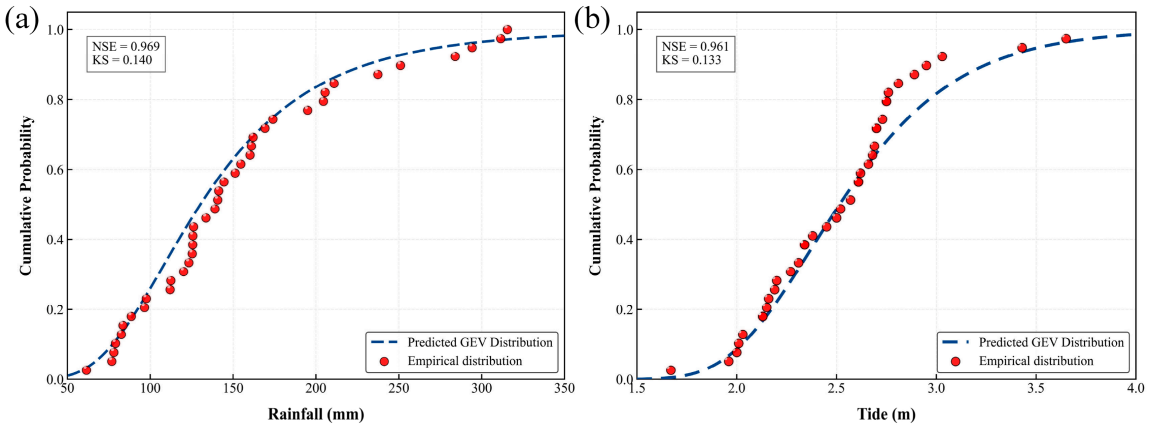

Figure 5. Comparison between empirical distribution and predicted GEV distribution. (**a**) Rainfall; (**b**) tide.

Table 4. Weights for models.

Events	Weight	
	TVPD Model	EC-Earth3-Veg Model
Rainfall	0.839	0.161

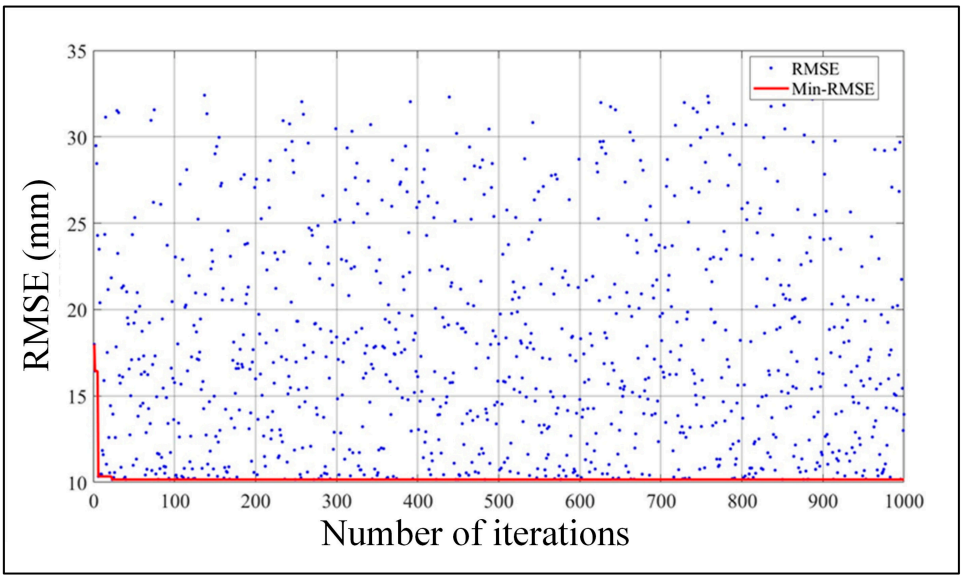

Figure 6. The evolution of the minimum RMSE.

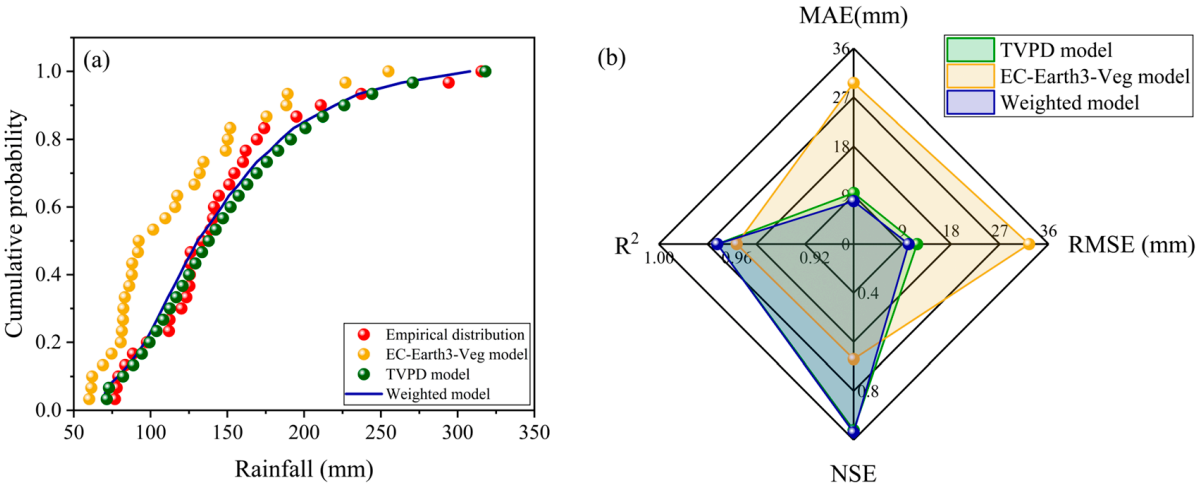

Figure 7. Comparison for models. (**a**) Cumulative probability; (**b**) error comparison.

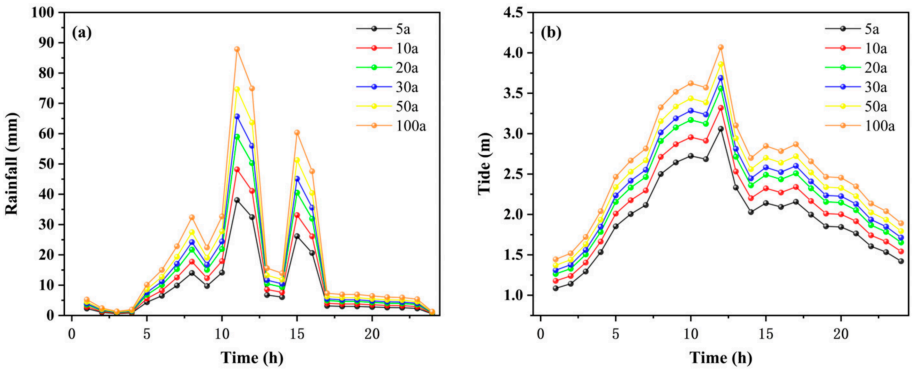

Figure 8. Designed series of rainfall and tides for different return periods. (**a**) Rainfall; (**b**) tides.

4.2. Accuracy Assessment of Land Use Model and Future Land Use Prediction

4.2.1. The Validation of Land Use Model

In this study, the Markov–PLUS model with a sampling rate of 50% was used to simulate land use in the main urban area of Haikou City in 2023. Based on the Markov Chain model, this study utilized historical land use data to derive the transition probability matrix among various land use types, which served as the foundation for the quantitative prediction of future land use evolution. The transition probability matrix objectively reflects the inherent mechanism by which the system maintains its historical evolutionary trend in the absence of abrupt intervention from major external policies. The conversion probabilities for each land use type under the natural development scenario are listed in Table 5.

Table 5. Probability of land use conversion for various land types under the natural development scenario.

Type	Water	Forest	Cropland	Artificial Surface	Grassland
Water	0.791118	0.023312	0	0.171482	0.014088
Forest	0.025338	0.874398	0	0.049433	0.050832
Cropland	0.031785	0.002445	0.022005	0.075795	0.867971
Artificial surface	0.002485	0.003017	0.000515	0.991701	0.002282
Grassland	0.04529	0.05066	0.002918	0.18653	0.714603

Table 6 presents the comparison between the simulated land-use demand and the actual 2023 land-use data in the main urban area of Haikou City. The low overall relative error (1.07%) demonstrates that the Markov-chain-based land-use demand prediction is accurate and reliable, indicating that the predicted land-use demand can serve as a suitable input for subsequent simulation experiments.

Table 6. Accuracy validation results of the Markov Chain.

Type	Simulation for 2023 (km^2)	ESA Data for 2023 (km^2)	Error (km^2)	Overall Error
Water	1.2721	1.3668	0.0947	
Forest	0.6032	0.8864	0.2832	
Cropland	0.0318	0.0457	0.0139	1.07%
Artificial surface	82.3396	81.9172	0.4224	
Bare land	0.0346	0	0.0346	

In the Land Expansion Analysis Strategy (LEAS) module, the sampling mode was set to random sampling, the number of decision trees was set to 100, and the sampling rate was assigned as 0.1. The number of features adopted for random forest training was limited to no more than the number of driving factors, which was specified as 15. The root mean square errors obtained from random forest training for each land use type were 0.119 for water bodies, 0.125 for forestland, 0.054 for cultivated land, 0.154 for artificial surfaces, 0.050 for bare land, and 0.125 for grassland, with the simulation accuracy fully satisfied. The land use transition matrix serves as a dominant influencing factor for land use change, which determines whether conversion between different land use types is permissible. A matrix value of 1 was assigned when conversion was allowed, while a value of 0 was set when conversion was prohibited. The land use transition matrix was established according to the actual land use conditions of the study area, combined with variations in model simulation accuracy, with detailed results presented in Table 7. The neighborhood factor parameters for water, forests, cropland, artificial surfaces, bare land, and grassland were set to 0.27, 0.10, 0.11, 0.45, 0.03, and 0.04, respectively, based on the proportion of the expanded

area of each land use type compared to the total expanded area of the land during the period 2017–2020. Finally, when comparing the predicted land use with the actual land use in 2023 (as shown in Figure 9), the Kappa coefficient and FOM values were obtained as 0.79 and 0.15 (as shown in Table 8), respectively, and the simulation results can be considered reasonable [32,33]. Therefore, the model was adopted to predict future land use in the main urban area of Haikou City.

Table 7. The transition matrix for land use.

Type	Water	Forest	Cropland	Artificial Surface	Bare Land	Grassland
Water	1	1	1	1	0	1
Forest	0	1	1	0	0	0
Cropland	1	1	1	0	0	1
Artificial surface	0	1	1	1	0	1
Bare land	1	1	1	1	1	1
Grassland	1	1	1	1	0	1

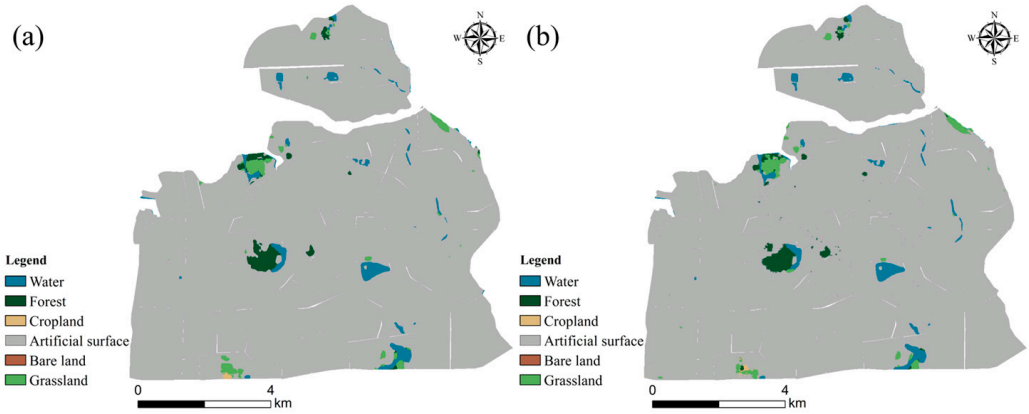

Figure 9. Comparison between the historical land use data in 2023 and the model of predicted land use data for 2023. (**a**) Historical land use; (**b**) model of predicted land use.

Table 8. Accuracy validation results of the land use model.

Parameters	Kappa	FOM
Value	0.79	0.15

4.2.2. Land Use Prediction

The land use transition probability matrix was adjusted according to the natural development scenario, enabling the quantities of various land use categories to be calculated using the Markov Chain in the main urban area of Haikou City for 2035 (as shown in Table 9). Figure 10 shows the final prediction results of land use in 2035 under the natural development scenario. The results demonstrate that the overall land use structure of the main urban area of Haikou City in 2035 is similar to the land use structure in 2023, which is dominated by artificial surface. The expansion of green spaces was prioritized by the Haikou Government due to its emphasis on ecological conservation, resulting in a reduction in impervious surfaces and a concurrent increase in pervious areas. Compared to 2023, the water area decreased by 0.02 km^2, forest areas increased by 0.71 km^2, artificial surfaces decreased by 0.83 km^2, and grassland increased by 0.14 km^2 in 2035 (see Figure 10b).

Table 9. Quantities of future land use categories for the study area under a natural development scenario (hundred m^2).

Year	Water	Forest	Cropland	Artificial Surface	Bare Land	Grassland
2023	13,668	8864	457	819,172	0	8876
2035	13,465	15,953	458	810,856	0	10,306

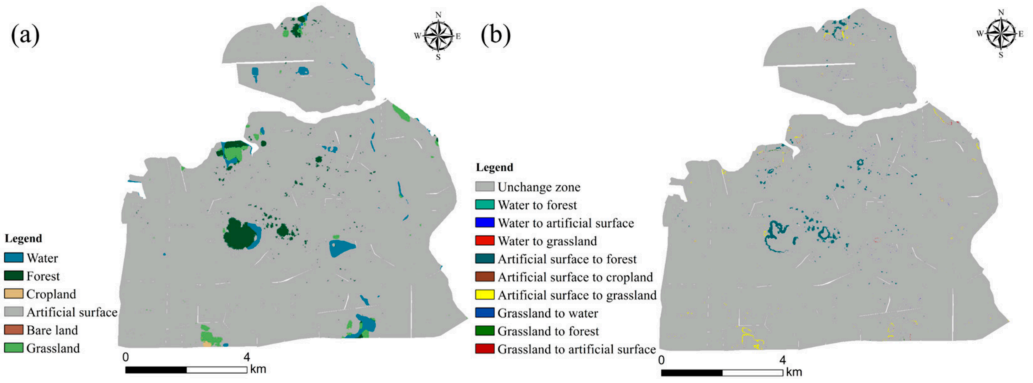

Figure 10. Land use changes under the natural development scenario in the future. (**a**) Future land use under natural development scenario; (**b**) land use change.

4.3. Influence on Flood Inundation Under Future Scenarios

4.3.1. Calibration of Urban Flood Inundation Model

The parameters of the urban flood inundation model were calibrated using observations from Typhoon Rammasun in July 2014. Figure 11 compares the observed and simulated water depths at various monitoring points. Although discrepancies exist due to data limitations, such as terrain accuracy, the differences are generally small. The relative errors at all points are below 10%, and the NSE value is 0.796, indicating that the model is suitable for simulating urban flooding. Thus, the model is considered acceptable for urban flooding simulation [34].

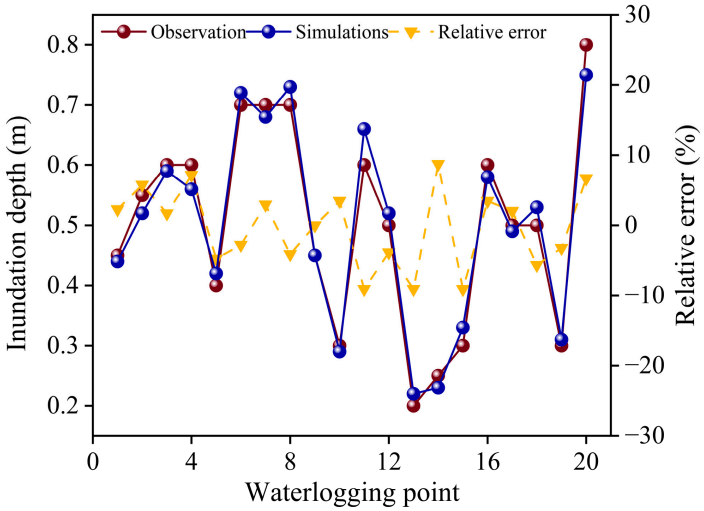

Figure 11. Observed and simulated inundation depth of observation points.

4.3.2. Impact of Rainfall and Tide Changes on Flood Inundation

We analyzed the impact of rainfall and tide changes on flood inundation based on the differences in flood simulation results between future and base periods. Figure 12 shows the results of a compound flood simulation for the 72 simulation scenarios, which

indicate that the flood inundation in the study area is severe under rainfall and tide changes. Figures 12 and 13 provide a comparison of the extent of the compound flood in the study area under different scenarios. Under the climate change scenarios, the average maximum inundation volume was estimated to be 6.5733 million m^3, representing an increase of 1.1431 million m^3, or 21.05%, compared with the baseline scenario. In terms of the inundation extent, the average inundation area increased from 16.63 km^2 under the baseline scenario to 18.71 km^2 under the climate change scenario, corresponding to an increase of 2.08 km^2, or approximately 12.51%. For instance, the peak inundation volume increased by 1.73 million m^3 compared with the base period scenarios under the combined rainfall–tide return period of 50 years (as shown in Figure 12). The peak inundation extent increased by 4.5 million m^2 compared with the base period scenarios. In addition, the significantly inundated extents remain largely consistent between the base and future period scenarios, exhibiting significant expansion when exceeding the combined RP of 50 years (Figure 13).

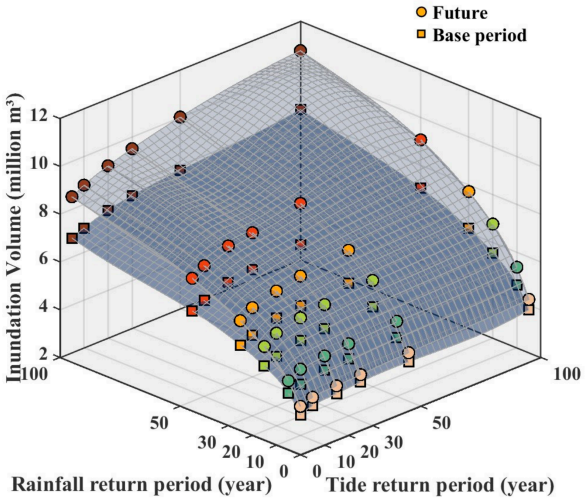

Figure 12. Changes in compound flood inundation volume under rainfall and tide changes.

4.3.3. Impact of Land Use, Rainfall, and Land Tide Changes on Flood Inundation

On the basis of rainfall and tide simulations, the land use change was input to simulate the flood inundation under future scenarios. Figure 14 presents the results of changes in compound flood inundation volume under rainfall, tide and land use changes. The results in Figure 14b indicate that the future peak inundation volume exceeds that in the baseline period. Specifically, under the climate and land-surface change scenario, the average maximum inundation volume was estimated to be 6.515 million m^3, representing an increase of 1.0847 million m^3, or 19.97%, compared with the baseline period. For instance, the peak inundation volume under the future scenario increased by 1.67 million m^3 compared to the base period scenario for the combined rainfall tide RP of 50 years. However, the peak inundation volume was reduced under combined variations in rainfall, tide and land use compared to scenarios with rainfall and tide variations (see Figures 12 and 14b). For example, the peak inundation volume was reduced by 0.12 million m^3 compared to scenarios with variations in rainfall and tides for the combined RP of 100 years. Therefore, rainfall, tide and land use changes are incorporated into the flood prediction framework, enabling more accurate prediction of future compound flood inundation changes in coastal cities.

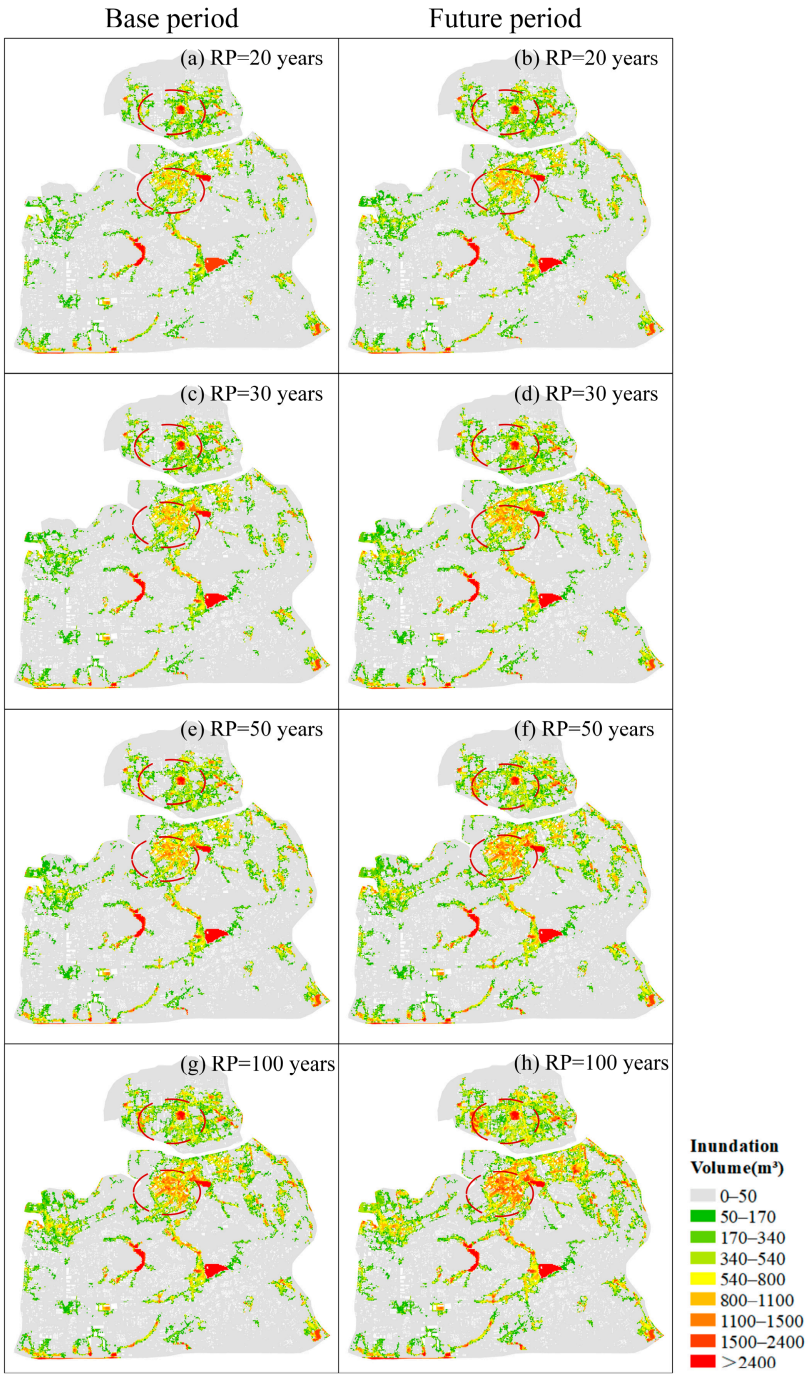

Figure 13. Changes in compound flood inundation area under rainfall and tide changes.

Compared with the scenario considering rainfall and tide changes only, incorporating future land use changes slightly reduced the projected peak inundation volume. This is mainly because the predicted 2035 land use pattern shows a decrease in artificial surfaces and an increase in forest and grassland areas, which may enhance infiltration and surface storage. The land surface change plays an important regulating role in future compound flood prediction, although rainfall and tide changes remain the dominant drivers. Therefore, changes in rainfall, tide, and land use can all substantially influence urban flood dynamics and should not be neglected in urban flood risk prediction.

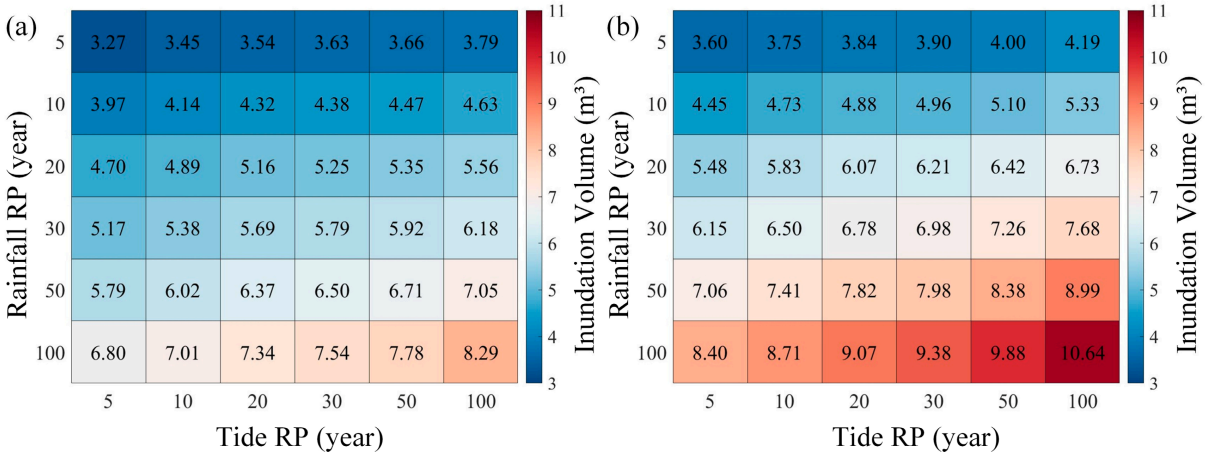

Figure 14. Changes in compound flood inundation volume under rainfall, tide and land use changes. (**a**) Base period; (**b**) future period.

4.4. Impact of Compound Flood on Socioeconomic Under Future Scenarios

4.4.1. Affected Population and GDP of Compound Flood Under Future Scenarios

Human casualties and economic losses are typically caused by floods, making the prediction of affected populations and economic metrics in high-risk areas critical for flood management strategies. Research confirmed that the events induce substantial population and economic consequences when inundation depth reaches 0.15 m [1]. In this study, the affected population and GDP were predicted by the flood simulation and projected future population and GDP distribution. Figure 15 illustrates that the affected population and GDP to compound flood increase significantly with changes in land use, rainfall and tides under future scenarios. The affected population and GDP to compound flood are predicted under future scenarios compared to the base period scenarios, with mean increases of 72,603 people and US$12.61 billion, respectively. Figure 16 demonstrates the distribution of the affected population and GDP of compound floods under future and base period scenarios, indicating that areas affected by population and GDP are increasing significantly. These results suggest that the population and GDP face substantial threats under non-stationary environments.

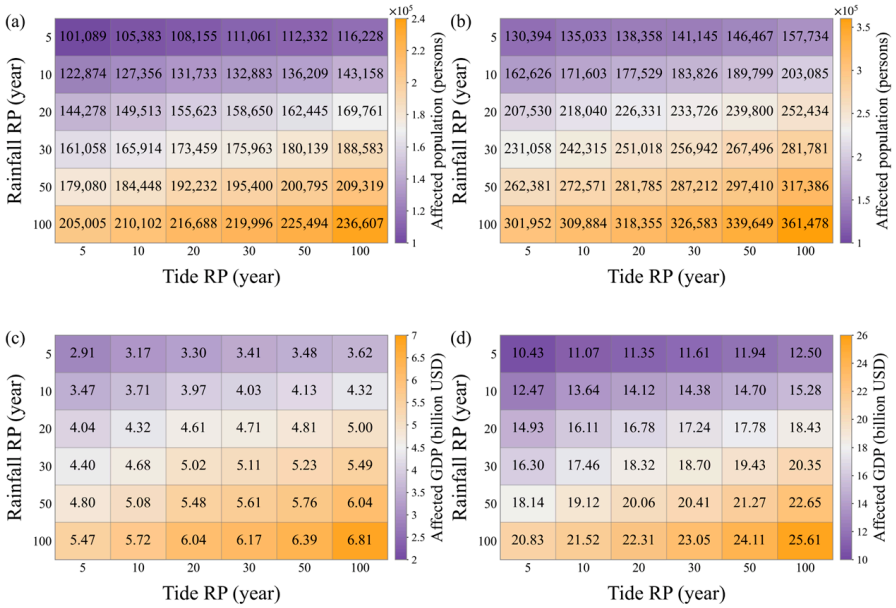

Figure 15. Affected population and GDP. (**a**) Base period population. (**b**) Future population. (**c**) Base period GDP, 2005 PPP USD. (**d**) Future period GDP, 2005 PPP USD.

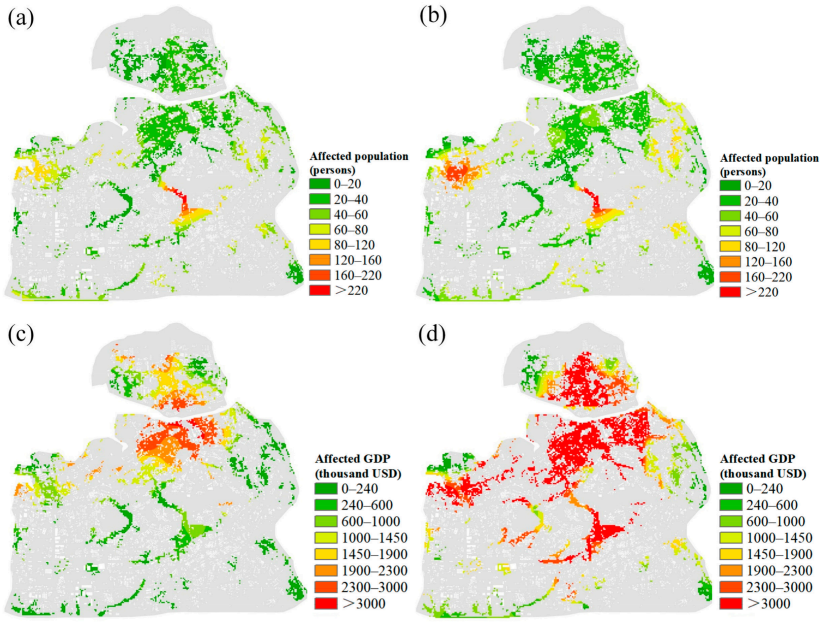

Figure 16. Affected population and GDP distribution for rainfall–tide RP of 100 years. (**a**) Base period population distribution. (**b**) Future population distribution. (**c**) Base period GDP distribution, 2005 PPP USD. (**d**) Future GDP distribution, 2005 PPP USD.

4.4.2. Impact of Compound Flood on Socioeconomic Risk Under Future Scenarios

In this paper, the population and GDP distributions within inundation areas above 0.15 m were peak-minimum normalized by ArcGIS under base and future periods to account for compound flood impacts on socioeconomic risk. And the weight of 0.5 was assigned to the population and GDP, respectively. Figure 17 shows the impact of compound floods on the socioeconomic risk, which indicates that the socioeconomic risk of the future scenario is higher overall than the base period scenario. The peak socioeconomic risk escalates from 0.63 in the base period to 0.79 in the future under a combined RP of 100 years, which increases by 25.4%. The high-risk areas are predominantly concentrated in three sectors: the northwestern coastal sector of the urban area, the interface between Haidian Island and the primary urban area, and the central region in the study area (as shown in Figure 17). The changes in socioeconomic risk provide options for developing flood prevention strategies to guard against areas with elevated socioeconomic risks in future scenarios, and for upgrading drainage facilities to enhance the area's resilience to risks.

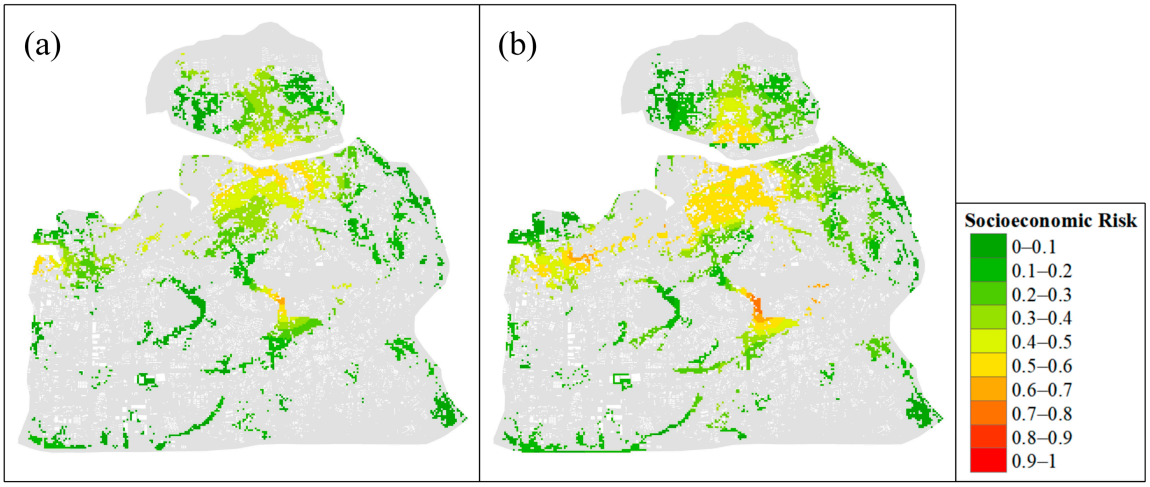

Figure 17. Impact of compound floods on socioeconomic risk. (**a**) Base period; (**b**) future period.

The projected increase in socioeconomic risk is not only related to the expansion of flood inundation, but also to the spatial redistribution of future population and economic assets. Even where the increase in inundation extent is moderate, higher population density and GDP concentration within flood-prone areas can substantially amplify the potential consequences of flooding. This explains why the future socioeconomic risk index shows a marked increase under high-return-period compound events. This finding agrees with previous studies suggesting that future flood risk is jointly shaped by changes in hazard intensity and exposure patterns. Global and regional studies have reported that rapid urban growth in flood-prone zones can significantly increase population and asset exposure, even when flood hazard changes are relatively limited. Similarly, studies on climate and population change have shown that future flood losses may rise because socioeconomic development increases the concentration of people and economic activities in vulnerable areas.

4.5. Limitations and Future Works

This study proposed an urban flood forecasting framework for coastal cities under a non-stationary environment, and investigated the effect of rainfall, tide and land surface changes on flood inundation and socioeconomic risk. However, this study has several limitations. For instance, due to data limitations, we applied the proposed framework to Haikou City. In future work, regional SLR projections and land subsidence data should be explicitly incorporated into the tide boundary conditions to improve the physical representation of future coastal water levels. And with the collection of additional data, this approach could be extended to project the flood risk for coastal China and even globally. Furthermore, based on the flood risk prediction, we will focus on evaluating flood mitigation strategies for coastal cities, including seawall elevation and sewer system capacity upgrades in our future work. Nevertheless, the equal-weighting scheme may influence the resulting socioeconomic risk index. Future studies should further examine the sensitivity of the risk index to different weighting schemes and investigate the relative importance of population and economic indicators under different socioeconomic development scenarios. And the EC-Earth3-Veg was selected because of its relatively good performance in simulating precipitation over China; the use of a single CMIP6 model may still introduce uncertainty into future rainfall projections. Different GCMs can produce divergent estimates of future rainfall intensity and frequency due to differences in model structures, parameterizations, and climate sensitivity. Such uncertainty may further propagate into the design of rainfall, flood inundation simulation, and socioeconomic risk assessments. Therefore, future studies should incorporate multi-model CMIP6 ensembles and multiple SSP scenarios to quantify the uncertainty range of future rainfall projections and to improve the robustness of compound flood risk prediction.

5. Conclusions

This paper developed a compound flood prediction framework to assess the effects of rainfall, tide and land surface changes on flood inundation and socioeconomic risks under a non-stationary environment. Future rainfall was predicted by integrating the TVPD model with EC-Earth3-Veg rainfall data through the genetic algorithm, while future tides were estimated using the TVPD model. The PLUS model was used to predict future land use. Based on the urban flood inundation model, the flooding simulation was employed to analyze the compound flood risk.

The integrated rainfall prediction model improved the agreement with the empirical distribution, reducing RMSE by 13.4% compared with individual models. The flood inundation and socioeconomic risk were predicted in the main urban area of Haikou City under

the design future scenarios. The results revealed that the future peak inundation volume exceeds the base period, with an average increase of 18.5% under rainfall, tide and land use changes. The socioeconomic risk from compound floods is increasingly exacerbated under the non-stationary environment, leading to an average rise of 72,603 more people exposed to flooding and US$12.61 billion in additional exposure.

Author Contributions: H.X.: Writing—review and editing, Supervision, Methodology, Conceptualization, and Funding acquisition. J.Z.: Writing—review and editing, Writing—original draft, Validation, Software, Methodology, and Data curation. H.W.: Supervision, Methodology, and Funding acquisition. Y.G.: Validation. Y.D.: Validation. Y.Z.: Validation. All authors have read and agreed to the published version of the manuscript.

Funding: This research was supported by the Excellent Youth Foundation of Henan Province Scientific Committee (grant number 242300421038); the Young Elite Scientists Sponsorship Program by HAST (grant number 2025HYTP031); and Scientific and Technological Projects of Henan Province (grant number 262102321158).

Data Availability Statement: The original contributions presented in this study are included in the article. Further inquiries can be directed to the corresponding author.

Conflicts of Interest: The authors declare that they have no known competing financial interests or personal relationships that could have appeared to influence the work reported in this paper.

References

1. Rentschler, J.; Salhab, M.; Jafino, B.A. Flood exposure and poverty in 188 countries. *Nat. Commun.* **2022**, *13*, 3527. [CrossRef]
2. Jang, J.H.; Chang, T.H. Flood risk estimation under the compound influence of rainfall and tide. *J. Hydrol.* **2022**, *606*, 127446. [CrossRef]
3. Xu, K.; Wang, C.Y.; Bin, L.L.; Shen, R.Z.; Zhuang, Y.C. Climate change impact on the compound flood risk in a coastal city. *J. Hydrol.* **2023**, *626*, 130237. [CrossRef]
4. Nicholls, R.J.; Lincke, D.; Hinkel, J.; Brown, S.; Vafeidis, A.T.; Meyssignac, B.; Hanson, S.E.; Merkens, J.L.; Fang, J.Y. A global analysis of subsidence, relative sea-level change and coastal flood exposure. *Nat. Clim. Change* **2021**, *11*, 338–342. [CrossRef]
5. Rogers, J.S.; Maneta, M.P.; Sain, S.R.; Madaus, L.E.; Hacker, J.P. The role of climate and population change in global flood exposure and vulnerability. *Nat. Commun.* **2025**, *16*, 1287. [CrossRef] [PubMed]
6. Miller, J.D.; Hutchins, M. The impacts of urbanisation and climate change on urban flooding and urban water quality: A review of the evidence concerning the United Kingdom. *J. Hydrol. Reg. Stud.* **2017**, *12*, 345–362. [CrossRef]
7. Wu, Y.; Haigh, I.D.; Gao, C.; Jenkins, L.J.; Green, J.; Jane, R.; Xu, Y.; Hu, H.; Wu, N. Compound Flooding Potential from the Joint Occurrence of Precipitation and Storm Surge in the Qiantang Estuary, China. *J. Hydrometeorol.* **2024**, *25*, 735–753. [CrossRef]
8. Xu, H.; Ragno, E.; Jonkman, S.N.; Wang, J.; Bricker, J.D.; Tian, Z.; Sun, L. Combining statistical and hydrodynamic models to assess compound flood hazards from rainfall and storm surge: A case study of Shanghai. *Hydrol. Earth Syst. Sci.* **2024**, *28*, 3919–3930. [CrossRef]
9. Zhou, Q.; Teng, S.; Situ, Z.; Liao, X.; Feng, J.; Chen, G.; Zhang, J.; Lu, Z. A deep-learning-technique-based data-driven model for accurate and rapid flood predictions in temporal and spatial dimensions. *Hydrol. Earth Syst. Sci.* **2023**, *27*, 1791–1808. [CrossRef]
10. Lee, C.-C.; Huang, L.; Antolini, F.; Garcia, M.; Juan, A.; Brody, S.D.; Mostafavi, A. Predicting peak inundation depths with a physics informed machine learning model. *Sci. Rep.* **2024**, *14*, 14826. [CrossRef]
11. Bates, P.D.; Quinn, N.; Sampson, C.; Smith, A.; Wing, O.; Sosa, J.; Savage, J.; Olcese, G.; Neal, J.; Schumann, G.; et al. Combined Modeling of US Fluvial, Pluvial, and Coastal Flood Hazard Under Current and Future Climates. *Water Resour. Res.* **2021**, *57*, e2020WR028673. [CrossRef]
12. Wei, Z.; Villarini, G.; Vecchi, G.A.; Smith, J.A. Urbanization exacerbated the rainfall and flooding caused by hurricane Harvey in Houston. *Nature* **2018**, *563*, 384–388. [CrossRef]
13. Guan, X.J.; Xia, C.; Xu, H.S.; Liang, Q.H.; Ma, C.; Xu, S.L. Flood risk analysis integrating of Bayesian-based time-varying model and expected annual damage considering non-stationarity and uncertainty in the coastal city. *J. Hydrol.* **2023**, *617*, 129038. [CrossRef]
14. Lee, H.; Calvin, K.; Dasgupta, D.; Krinner, G.; Mukherji, A.; Thorne, P.W.; Trisos, C.; Romero, J.; Aldunce, P.; Barrett, K.; et al. *Climate Change 2023: Synthesis Report. Contribution of Working Groups I, II and III to the Sixth Assessment Report of the Intergovernmental Panel on Climate Change*; IPCC: Geneva, Switzerland, 2023. [CrossRef]

15. Yuan, H.H.; Ning, L.K.; Zhou, J.W.; Shi, W.; Huang, J.B.; Luo, Y. HiCPC: A new 10-km CMIP6 downscaled daily climate projections over China. *Sci. Data* **2024**, *11*, 1167. [CrossRef]
16. Giorgi, F. Thirty Years of Regional Climate Modeling: Where Are We and Where Are We Going next? *J. Geophys. Res. Atmos.* **2019**, *124*, 5696–5723. [CrossRef]
17. Rentschler, J.; Avner, P.; Marconcini, M.; Su, R.; Strano, E.; Vousdoukas, M.; Hallegatte, S. Global evidence of rapid urban growth in flood zones since 1985. *Nature* **2023**, *622*, 87–92. [CrossRef]
18. Barati, A.A.; Zhoolideh, M.; Azadi, H.; Lee, J.H.; Scheffran, J. Interactions of land-use cover and climate change at global level: How to mitigate the environmental risks and warming effects. *Ecol. Indic.* **2023**, *146*, 109829. [CrossRef]
19. Liang, X.; Guan, Q.F.; Clarke, K.C.; Liu, S.S.; Wang, B.Y.; Yao, Y. Understanding the drivers of sustainable land expansion using a patch-generating land use simulation (PLUS) model: A case study in Wuhan, China. *Comput. Environ. Urban Syst.* **2021**, *85*, 101569. [CrossRef]
20. Zou, B.W.; Fan, C.L.; Li, J.J.; Wang, M.; Liao, Y.D.; Zhou, X.Q. Assessing the impact of land use changes on urban heat risk under different development scenarios: A case study of Guangzhou in China. *Sustain. Cities Soc.* **2025**, *130*, 106532. [CrossRef]
21. Liu, J.F.; Kong, X.L.; Zhu, Y.; Zhang, B.H. A study on land use change simulation based on PLUS model and the U-net structure: A case study of Jilin Province. *Ecol. Indic.* **2025**, *176*, 113619. [CrossRef]
22. Wu, J.H.; Wang, H.W.; Wang, C.; Huang, X.; Wei, J.X.; Wang, Z.G.; Zhang, C.; Chen, B.; Yiming, Y.; Lei, C.; et al. Zoning and spatial resilience: Land use and food security in the Ili River Valley, China. *Land Use Policy* **2025**, *157*, 107657. [CrossRef]
23. Bender, J.; Wahl, T.; Jensen, J. Multivariate design in the presence of non-stationarity. *J. Hydrol.* **2014**, *514*, 123–130. [CrossRef]
24. Molina Bacca, E.J.; Stevanović, M.; Bodirsky, B.L.; Doelman, J.C.; Parsons Chini, L.; Volkholz, J.; Frieler, K.; Reyer, C.P.O.; Hurtt, G.; Humpenöder, F.; et al. Future land-use pattern projections and their differences within the ISIMIP3b framework. *Earth Syst. Dyn.* **2025**, *16*, 753–801. [CrossRef]
25. Xu, H.S.; Zhang, X.; Guan, X.J.; Wang, T.Y.; Ma, C.; Yan, D.H. Amplification of Flood Risks by the Compound Effects of Precipitation and Storm Tides Under the Nonstationary Scenario in the Coastal City of Haikou, China. *Int. J. Disaster Risk Sci.* **2022**, *13*, 602–620. [CrossRef]
26. Wang, X.Y.; Meng, X.F.; Long, Y. Projecting 1 km-grid population distributions from 2020 to 2100 globally under shared socioeconomic pathways. *Sci. Data* **2022**, *9*, 563. [CrossRef] [PubMed]
27. Wang, T.T.; Sun, F.B. Global gridded GDP data set consistent with the shared socioeconomic pathways. *Sci. Data* **2022**, *9*, 221. [CrossRef]
28. Cheng, L.Y.; AghaKouchak, A.; Gilleland, E.; Katz, R.W. Non-stationary extreme value analysis in a changing climate. *Clim. Change* **2014**, *127*, 353–369. [CrossRef]
29. Xu, H.; Chen, H.; Wang, H. Future changes in precipitation extremes across China based on CMIP6 models. *Int. J. Climatol.* **2021**, *42*, 635–651. [CrossRef]
30. Lian, J.J.; Xu, H.S.; Xu, K.; Ma, C. Optimal management of the flooding risk caused by the joint occurrence of extreme rainfall and high tide level in a coastal city. *Nat. Hazards* **2017**, *89*, 183–200. [CrossRef]
31. Zhuang, Y.C.; Xu, K.; Bin, L.L.; Ma, C.; Zhang, J.L.; Lian, J.J. Identifying and assessing the jacking effect under compound flooding in a coastal city using particle tracking method. *J. Hydrol.* **2025**, *657*, 133180. [CrossRef]
32. Xu, W.B.; Xu, H.Z.; Li, X.Y.; Qiu, H.; Wang, Z.Y. Ecosystem services response to future land use/cover change (LUCC) under multiple scenarios: A case study of the Beijing-Tianjin-Hebei (BTH) region, China. *Technol. Forecast. Soc. Change* **2024**, *205*, 123525. [CrossRef]
33. Wu, Q.; Wang, L.; Wang, T.Y.; Ruan, Z.Y.; Du, P. Spatial-temporal evolution analysis of multi-scenario land use and carbon storage based on PLUS-InVEST model: A case study in Dalian, China. *Ecol. Indic.* **2024**, *166*, 112448. [CrossRef]
34. Dechmi, F.; Burguete, J.; Skhiri, A. SWAT application in intensive irrigation systems: Model modification, calibration and validation. *J. Hydrol.* **2012**, *470*, 227–238. [CrossRef]

Disclaimer/Publisher's Note: The statements, opinions and data contained in all publications are solely those of the individual author(s) and contributor(s) and not of MDPI and/or the editor(s). MDPI and/or the editor(s) disclaim responsibility for any injury to people or property resulting from any ideas, methods, instructions or products referred to in the content.